

Supporting Information:

Origin of Low Carrier Mobilities in Halide Perovskites

Samuel Poncé,[†] Martin Schlipf,[†] and Feliciano Giustino^{*,†,‡}

[†]*Department of Materials, University of Oxford, Parks Road, Oxford OX1 3PH, United Kingdom*

[‡]*Department of Materials Science and Engineering, Cornell University, Ithaca, New York 14853, USA*

E-mail: feliciano.giustino@materials.ox.ac.uk

1 Soft modes contribution

In order to estimate the importance of the soft modes in cubic CsPbI₃ for the calculation of mobility, we repeated the calculations by setting the energy of the soft modes to $\hbar\omega = 1$ meV. The resulting electron and hole mobilities at 300 K are 80 cm²/Vs and 66 cm²/Vs, respectively. These values are almost identical to those obtained in the main text by neglecting the soft modes altogether. We conclude that the electron-phonon coupling to the soft modes in CsPbI₃ can be neglected when calculating carrier mobilities.

2 Scaling law

We here consider an idealized system with a parabolic band of mass m^* coupled to a single LO phonon of energy $\hbar\omega_{\text{LO}}$. The coupling strength is given by the dimensionless polaron

constant α :¹

$$\alpha = \frac{e^2}{\hbar \varepsilon_0} \left(\frac{m^*}{2\hbar \omega_{\text{LO}}} \right)^{1/2} \left(\frac{1}{\epsilon^\infty} - \frac{1}{\epsilon^0} \right), \quad (\text{S1})$$

where ϵ^0 and ϵ^∞ are the static and high-frequency relative dielectric constants, respectively, and ε_0 is the vacuum permittivity. Under these assumption the isotropic average of the mobility in Eq. (1) can be written as:

$$\mu = \frac{e \langle \tau \rangle}{m^*}, \quad (\text{S2})$$

with the average scattering rate given by:

$$\langle \tau \rangle = \frac{4}{3\sqrt{\pi}} \int_0^\infty dx x^{3/2} \exp(-x) \tau(x). \quad (\text{S3})$$

The scattering rate $\tau(x)$ in this expression is to be obtained from Eq. (2) of the main text, and $x = \varepsilon/k_{\text{B}}T$ represents the electron energy in units of the thermal energy. Figure S5 shows that the weight $x^{3/2} \exp(-x)$ in the above expression reaches a maximum at $x = 3/2$. Therefore, if we want to analyze trends in the carrier mobilities by focusing on a single electronic state, the most relevant electron energy is $\varepsilon = 3/2 k_{\text{B}}T$. Based on this reasoning, in Fig. 3(a-c) of the manuscript we consider electrons at an energy of 39 meV from the conduction band edge (for $T = 300$ K). We choose the wavevectors as follows: $\mathbf{k} = 0.48(1, 1, 1)2\pi/a$ for CsPbI₃, $\mathbf{k} = 0.06(1, 0, 0)2\pi/a$ for MAPbI₃, and $\mathbf{k} = 0.04(0, 0, 1)2\pi/c$ for GaN. The results are not sensitive to the direction of \mathbf{k} .

In this simplified model Eq. (2) of the manuscript reduces to:

$$\frac{1}{\tau(\varepsilon; T)} = \frac{2}{\hbar} \alpha \hbar \omega_{\text{LO}} \varphi(x, x_0), \quad \varphi(x, x_0) = \text{Im} \frac{[n(x_0) + 1] \arcsin \sqrt{x/x_0} + n(x_0) \arcsin i \sqrt{x/x_0}}{\sqrt{x/x_0}}, \quad (\text{S4})$$

where the dimensionless variables $x = \varepsilon/k_{\text{B}}T$ and $x_0 = \hbar \omega_{\text{LO}}/k_{\text{B}}T$ have been introduced. In order to carry out the integral in (S3) explicitly, we approximate the function $\varphi(x, x_0)$

by a step function with the discontinuity at $x = x_0$. The values to the left of this step are approximated using $\varphi(x = 0, x_0)$, while the values to the right are approximated using the maximum of the function φ . A simple estimate of the maximum is found by using the large x/x_0 limit of (S4), yielding $\varphi(x, x_0) \simeq [2n(x_0) + 1] \log \left(2\sqrt{x/x_0} \right) / \sqrt{x/x_0}$. The scattering rate in (S4) is thus approximated as:

$$\frac{1}{\tau(\varepsilon; T)} = 2 \alpha \omega_{\text{LO}} \begin{cases} n(x_0), & \text{if } x < x_0 \\ \frac{2}{e} [2n(x_0) + 1], & \text{if } x > x_0. \end{cases} \quad (\text{S5})$$

By combining (S5) and (S3) we obtain:

$$\mu = \frac{e\hbar}{m_e k_B T} \frac{F(x_0)}{\alpha m^*/m_e}, \quad (\text{S6})$$

where the dimensionless function $F(x_0)$ is defined as:

$$F(x_0) = \frac{1}{4x_0} \frac{e}{2n(x_0) + 1} + \frac{4}{4x_0} \left[\frac{2}{3\sqrt{\pi}} e^{-x_0} \sqrt{x_0} (x_0 + 3/2) - \frac{1}{2} \text{erf}(\sqrt{x_0}) \right] \left[\frac{e/2}{2n(x_0) + 1} - \frac{1}{n(x_0)} \right]. \quad (\text{S7})$$

For the compounds considered in this work and temperatures between 100 K and 300 K, $x_0 = \hbar\omega_{\text{LO}}/k_B T$ falls between 0.1 and 3.5. In this range the function F can be approximated by the simple power law $F(x_0) = 0.052 x_0^{3.3} + 0.34$, with an error smaller than 2%. Within this approximation the mobility in (S6) is found to obey the dimensionless scaling law:

$$\frac{\mu}{e\hbar/m_e k_B T} = \frac{0.052 (\hbar\omega_{\text{LO}}/k_B T)^{3.3} + 0.34}{\alpha m^*/m_e}, \quad (\text{S8})$$

or equivalently:

$$\mu [\text{cm}^2/\text{Vs}] = \frac{7444}{T[\text{K}]} \frac{0.052 (\hbar\omega_{\text{LO}}/k_B T)^{3.3} + 0.34}{\alpha m^*/m_e}. \quad (\text{S9})$$

3 Sensitivity to the choice of semicore shells in the pseudopotential

When performing GW quasiparticle calculations for heavy elements using the pseudopotential method, it is important to assess the sensitivity of the result to the choice of the semicore shell of the pseudopotential, especially in relation to the exchange part of the self-energy.² For $\text{CH}_3\text{NH}_3\text{PbI}_3$, it has already been shown that including the Pb $5d$ or the I $4d$ semicore states in the pseudopotential changes the gap by -0.1 eV and $+0.4$ eV, respectively.³ In Ref. 4 it has been shown that when the I $4s$ and $4p$ states are included in the pseudopotential, the gap opening associated with the $4d$ states is almost exactly compensated. We perform analogous tests for Pb in CsPbI_3 , by including also the $5s$ and $5p$ states as valence electrons, and we observe a similar compensation effect. These tests are summarized in Table S1. In this table we see that the results obtained by considering pseudopotentials without semicore states for I and with $5s$, $5p$, and $5d$ semicore states for Pb are very similar to those obtained by considering the complete semicore shells for both elements. In all calculations we employ the former configuration as it is computationally less expensive.

4 Materials and Methods

Electronic ground state and lattice dynamics

We perform density-functional theory (DFT) calculations using pseudopotentials and planewaves, as implemented in the Quantum ESPRESSO package.⁵ For MAPbI_3 we employ the local density approximation (LDA), for CsPbI_3 and GaN we use the PBE generalized gradient approximation. We used norm-conserving pseudopotentials from the PseudoDojo repository.^{6,7} We use fully relativistic pseudopotentials throughout for electronic structure calculations. In the case of Pb the semicore $5s$, $5p$, and $5d$ electrons are included in the valence (see section S3), in the case of Ga we include the $2s$ and $2p$ semicore states. We use planewaves

kinetic energy cutoffs of 100 Ry for MAPbI₃ and CsPbI₃, and 120 Ry for GaN. The structural models are generated by optimizing the atomic coordinates, while retaining the crystal symmetry and experimental lattice parameters. We use $a = 8.836$ Å, $b = 12.581$ Å, and $c = 8.555$ Å for MAPbI₃,⁸ $a = 6.276$ Å for CsPbI₃,⁸ and $a = 3.189$ Å, $c = 5.186$ Å for GaN.⁹ We calculate phonons using DFPT, 2×2×2 Brillouin zone grids for MAPbI₃ and 4×4×4 grids for CsPbI₃ and GaN. For the calculation of the dielectric permittivity tensors and the Born effective charges in MAPbI₃, CsPbI₃ and GaN we employ denser grids with 4×4×4, 16×16×16 and 14×14×14 points, respectively. In all calculations we apply the acoustic sum rule to the interatomic force constants.¹⁰ In the case of MAPbI₃ and CsPbI₃ we perform DFPT calculations using scalar-relativistic pseudopotentials, which yield more accurate phonon dispersion relations as shown in Ref.¹¹

Quasiparticle GW corrections

We correct DFT band structures via the quasiparticle GW method, using the Yambo code.¹² For MAPbI₃ we employ a higher planewaves kinetic energy cutoff of 150 Ry, we evaluate the exchange self-energy and the polarizability using cutoffs of 80 Ry and 6 Ry, respectively, and perform the summations over empty states using 1000 bands.¹³ The frequency-dependence of the screened Coulomb interaction is described via the Godby-Needs plasmon-pole model,¹⁴ using a plasmon-pole energy of 18.8 eV. Since the DFT gap of lead halide perovskites is very small due to spin-orbit coupling,¹³ we go beyond the G_0W_0 approximation by including self-consistency on the eigenvalues. We apply self-consistency by using a strategy similar to Refs.,¹³ but with a wavevector-dependent scissor so as to obtain accurate effective masses. In the case of CsPbI₃ we employ planewaves cutoffs of 60 Ry and 15 Ry for the exchange self-energy and the polarizability, respectively, 500 bands for the calculation of the polarization, and 600 bands for the Green's function. For GaN we employ a higher planewaves kinetic energy cutoff of 260 Ry, the exchange cutoff is set to 120 Ry, the polarizability cutoff is 29 Ry, and we include 1500 bands in the summations. In this case the plasmon-pole energy

is set to 16.5 eV. In all cases the Brillouin zone is sampled via a $4 \times 4 \times 4$ unshifted grid, and the termination scheme of Ref.¹⁵ is employed to accelerate the convergence with respect to the number of empty states.

Electron-phonon interactions

We calculate electron-phonon matrix elements required and scattering rates in Eq. (2) using the EPW code¹⁶ of the Quantum ESPRESSO distribution, in conjunction with the wannier90 library.¹⁷ We include spin-orbit coupling in all calculations. In the case of MAPbI₃ we start from a $2 \times 2 \times 2$ Brillouin zone grid for the phonon wavevectors, and interpolate on a fine grid of 100,000 points following a Cauchy distribution centered at Γ and weighted according to their Voronoi volume. In the cases of CsPbI₃ and GaN we used Γ -centered Cauchy grids for phonons with 480,000 and 205,000 points, respectively. Detailed convergence tests are shown in Figure S1. The evaluation of the Dirac deltas in Eq. (2) is performed by using Lorentzian functions with a broadening parameter γ . Since the scattering rates depend linearly on this artificial parameter for $\gamma \rightarrow 0$, we extrapolate the results to $\gamma = 0$.^{18,19} This procedure is illustrated in Figure S2.

Analytical integration of scattering rates

In order to perform highly accurate integrals in Eqs. (1) and (2) we map the *ab initio* calculations into an exactly solvable multi-phonon model of the scattering rates $1/\tau_{n\mathbf{k}}$, which we recently developed and validated.¹⁹ In this model the scattering rate is given by:

$$\frac{1}{\tau_{n\mathbf{k}}} = \frac{4\pi^2 |\mathbf{k}|}{\hbar \Omega_{\text{BZ}} \varepsilon_{n\mathbf{k}}} \sum_{\pm, \nu} [n_{\nu} + (1 \pm \sigma_{\text{b}})/2] G_{\nu}^2 \text{Im} \arcsin \left(\frac{\mp \hbar \omega_{\nu} - i\eta}{\varepsilon_{n\mathbf{k}}} \right)^{-1/2}, \quad (\text{S10})$$

where $\sigma_{\text{b}} = \pm 1$ for valence and conduction bands, respectively, and the parameters G_{ν} , ω_{ν} ($\nu = 1, 2, 3$), and η are determined by fitting *ab initio* calculations over several temperatures and wavevectors near the band edges. Using (S10) we determine the scattering rates for

\mathbf{k} along the reciprocal lattice vectors, $\tau_{n\mathbf{k},\alpha}$, and then we generate the scattering rates for arbitrary \mathbf{k} via elliptical interpolation, $1/\tau_{n\mathbf{k}} = |\mathbf{k}|^{-1} [\sum_{\alpha} (k_{\alpha}/\tau_{n\mathbf{k},\alpha})^2]^{1/2}$. Figure S3 shows that this interpolation procedure reliably reproduces direct *ab initio* calculations. As a sanity check, we also compare the mobility obtained by calculating explicitly the *ab initio* scattering rates and those obtained using (S10) for the case of CsPbI₃. Figure S4 shows that the agreement between the two approaches is excellent.

Estimates of photoconductive gain and switching frequency

The photoconductive gain reported in Fig. 4(b) is estimated using $G = \tau\mu V/L^2$. In order to make a consistent comparison we used reference parameters for MAPbI₃, namely $V = 0.9$ V the applied voltage, $L = 449$ nm the active layer thickness,²⁰ and $\tau^{-1} = 3 \cdot 10^7$ s⁻¹ the reciprocal of the monomolecular recombination lifetime.²¹ Using these parameters and our calculated mobility at 300 K, we find a photoconductive gain $G = 1100$ for the cubic phase of MAPbI₃ (here approximated as CsPbI₃ at the lattice parameter of cubic MAPbI₃). This result is in good agreement with the gain $G = 1500$ measured at wavelengths between 450 and 800 nm.²⁰ The switching frequency shown in Fig. 4(b) is estimated using $f_T = \mu V_{DS}/2\pi L^2$, where $V_{DS} = 20$ V is the drain-source voltage and $L = 80$ μ m is the transistor channel length, taken from Ref.²²

Table S1: **Sensitivity of the calculated band gaps to semicore electrons.** Impact of the semicore states in Pb and I on the fundamental band gap of cubic CsPbI₃. ‘ $G_0W_0 + \Delta_{\mathbf{k}}$ ’ stands for a self-consistent scissor calculation, where the scissor correction is \mathbf{k} -dependent. The configuration employed in the present manuscript is highlighted in bold.

Pb valence config.	I valence config.	DFT (eV)	Band gap	
			G_0W_0 (eV)	$G_0W_0 + \Delta_{\mathbf{k}}$ (eV)
5d ¹⁰ 6s ² 6p ²	5s ² 5p ⁵	0.07	0.50	0.62
5d ¹⁰ 6s ² 6p ²	4d ¹⁰ 5s ² 5p ⁵	0.07	0.98	1.22
5d ¹⁰ 6s ² 6p ²	4s ² 4p ⁶ 4d ¹⁰ 5s ² 5p ⁵	0.07	0.47	0.60
5s ² 5p ⁶ 5d ¹⁰ 6s ² 6p ²	5s ² 5p ⁵	0.07	0.67	0.85
5s ² 5p ⁶ 5d ¹⁰ 6s ² 6p ²	4d ¹⁰ 5s ² 5p ⁵	0.08	1.20	1.50
5s ² 5p ⁶ 5d ¹⁰ 6s ² 6p ²	4s ² 4p ⁶ 4d ¹⁰ 5s ² 5p ⁵	0.08	0.68	0.88

Table S2: **Quasiparticle effective masses.** Effective masses and band gaps of MAPbI₃, CsPbI₃, and GaN calculated at various levels of approximation. ‘G₀W₀’ indicates one-shot GW calculations, ‘G₀W₀ + Δ’ indicates the self-consistent scissor method of Ref.,³ and the values reported for MAPbI₃ are taken from Ref.¹³ ‘G₀W₀ + Δ_{**k**}’ stands for a self-consistent scissor calculation, where the magnitude of the scissor correction varies across the Brillouin zone. This method yields results closest to a GW calculation with complete self-consistency on the eigenvalues (G₀W₀ + Δ_{**nk**}), and is employed in all present mobility calculations for perovskites.

Method	Hole effective mass (m_e)	Electron effective mass (m_e)	Band gap (eV)
Orthorhombic MAPbI ₃			
DFT	0.138	0.118	0.47
G ₀ W ₀	0.175	0.163	1.15
G ₀ W ₀ + Δ ³	0.230	0.240	1.57
G ₀ W ₀ + Δ _{k}	0.182	0.211	1.38
Cubic CsPbI ₃			
DFT	0.024	0.023	0.07
G ₀ W ₀	0.146	0.150	0.67
G ₀ W ₀ + Δ	0.150	0.157	0.75
G ₀ W ₀ + Δ _{k}	0.156	0.167	0.85
G ₀ W ₀ + Δ _{nk}	0.157	0.170	0.87
Wurtzite GaN			
DFT	2.47	0.193	1.93
G ₀ W ₀	3.20	0.204	2.83

Table S3: **Fröhlich coupling parameters.** Parameters used in the model of (S8) in order to construct the mobility map shown in Fig. 4. We give the calculated high-frequency (ϵ^∞) and static (ϵ^0) relative dielectric constants, the phonon energy of the principal LO mode ($\hbar\omega_{\text{LO}}$), the electron or hole effective mass, the calculated Fröhlich coupling constant (α), the polar mass ($\alpha m^*/m_e$), the reduced phonon frequency evaluated at room temperature ($\hbar\omega_{\text{LO}}/k_{\text{B}}T$), and the average electron and hole mobilities estimated using (S8) (μ^{model}) as well as those calculated entirely from first principles (μ^{full}).

Compound	ϵ^∞	ϵ^0	$\hbar\omega_{\text{LO}}$ meV	m^*/m_e	α	$\alpha m^*/m_e$	$\hbar\omega_{\text{LO}}/k_{\text{B}}T$	μ^{model} cm ² /Vs	μ^{full} cm ² /Vs
electrons									
MAPbI ₃	5.9	22.6	12.6	0.211	1.91	0.47	0.49	39	33
CsPbBr ₃	4.9	33.3	20.4	0.280	2.36	0.66	0.79	25	41
CsPbI ₃	6.3	53.2	15.8	0.167	1.69	0.28	0.61	57	76
CsSnBr ₃	7.6	45.1	19.3	0.168	1.20	0.20	0.75	82	89
CsSnI ₃	10.1	66.1	15.4	0.090	0.75	0.07	0.59	238	177
GaN	5.7	10.0	84.6	0.204	0.43	0.09	3.27	1502	811
holes									
MAPbI ₃	5.9	22.6	12.9	0.182	1.75	0.35	0.50	50	50
CsPbBr ₃	4.9	33.3	20.4	0.234	2.15	0.50	0.79	33	44
CsPbI ₃	6.3	53.2	15.8	0.156	1.63	0.25	0.61	63	61
CsSnBr ₃	7.6	45.1	19.3	0.111	0.97	0.11	0.75	153	241
CsSnI ₃	10.1	66.1	15.4	0.065	0.64	0.04	0.59	386	465

Table S4: ***Ab initio* parameters for the analytical interpolation of the scattering rates.** Parameters used in Eq. (3) of the manuscript. The parameters have been determined by fitting explicit calculations of the scattering rates at various temperatures along the indicated direction. The comparison between the analytical model of the scattering rates and direct calculations is performed in Figure S3.

	Direction	G_1^2 meV ² /Å ²	$\hbar\omega_1$ meV	G_2^2 meV ² /Å ²	$\hbar\omega_2$ meV	G_3^2 meV ² /Å ²	$\hbar\omega_3$ meV
MAPbI ₃ conduction	ΓX	8.7	5.7	79.8	13.4	85.1	19.2
	ΓY	7.9	5.1	45.7	9.7	78.5	15.3
	ΓZ	14.2	6.4	60.6	12.6	65.6	20.8
MAPbI ₃ valence	ΓX	3.5	3.6	76.1	12.6	87.0	17.9
	ΓY	5.0	3.9	75.0	12.2	79.0	18.6
	ΓZ	2.2	3.1	83.0	12.6	75.7	20.9
CsPbI ₃ conduction	RX	3.3	1.8	28.3	4.1	160	8.3
CsPbI ₃ valence	RX	4.9	1.9	22.0	4.6	171	8.2

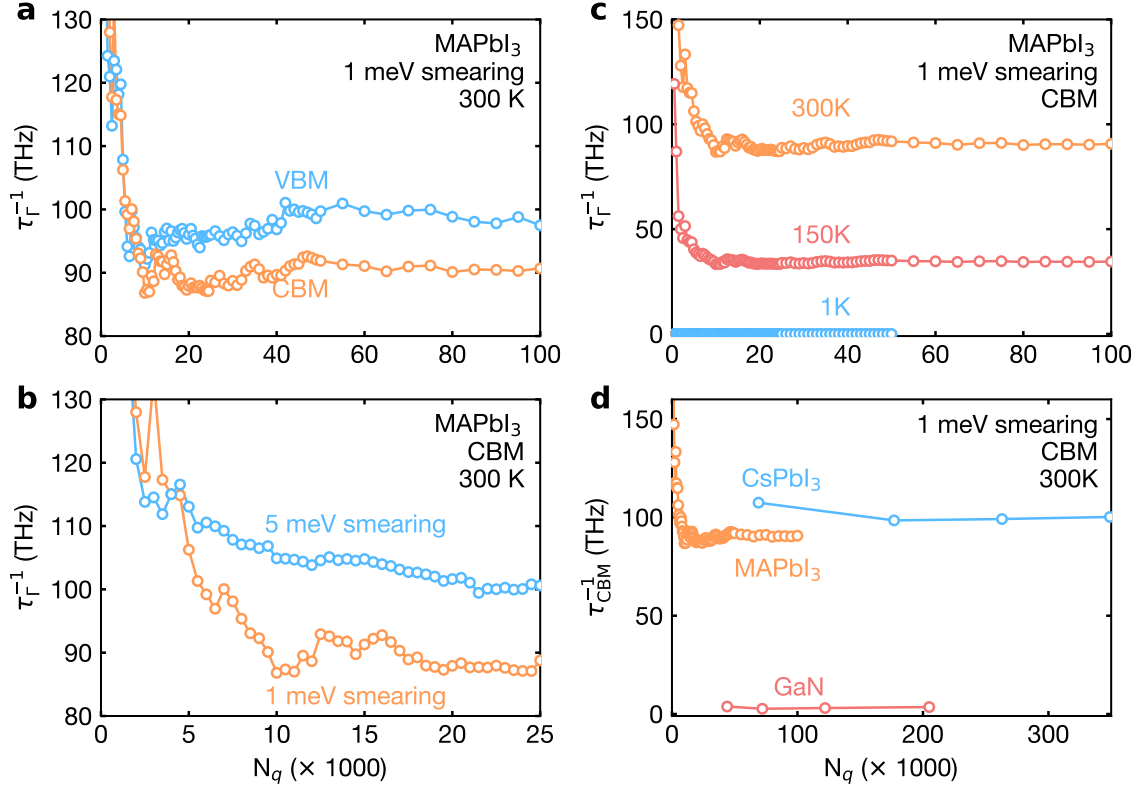


Figure S1: **Numerical convergence of the scattering rates with Brillouin zone sampling.** (a-c) Computed electron-phonon scattering rates in MAPbI₃ for electrons at the Γ point. (a) Comparison between the convergence rates of the conduction band minimum (CBM) and valence band maximum (VBM). (b) Sensitivity of the convergence rate to the Lorentzian broadening γ described in the methods. (c) Rate of convergence as a function of temperature. In all panels the number of grid points on the horizontal axis corresponds to a quasi-random Cauchy distribution. (d) Comparison between the convergence rates for MAPbI₃, CsPbI₃ and GaN at 300 K.

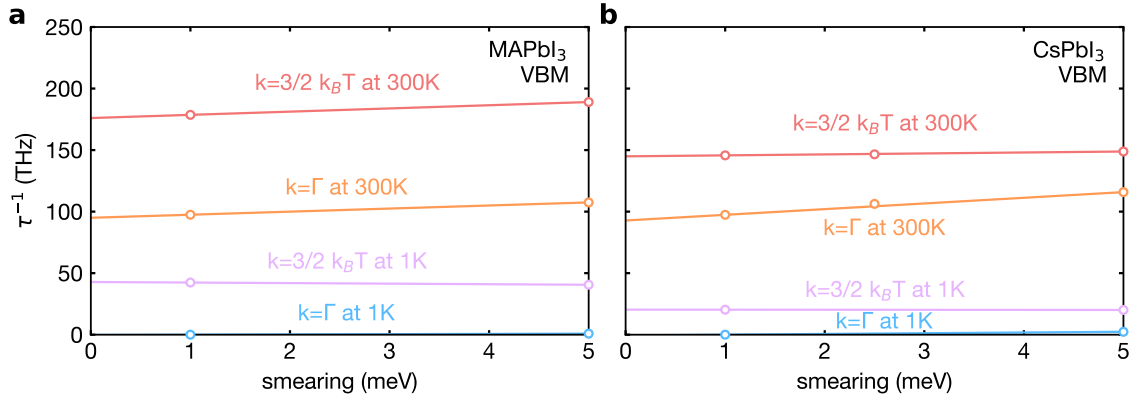


Figure S2: **Extrapolation of computed scattering rates to zero broadening.** The Dirac deltas in Eq. (2) of the manuscript are customarily replaced by Lorentzians for computational convenience. In order to avoid calculation artifacts arising from the artificial broadening of the Lorentzian peaks, we perform a careful extrapolation to vanishing broadening. **(a)** Extrapolation of representative scattering rates for MAPbI₃ (either at the valence band maximum at an energy $3/2k_B T$ away from it), at 1 K and 300 K. **(b)** Extrapolation of scattering rates for CsPbI₃, using the same color code as in (a). The circles represent explicit *ab initio* calculations, the lines are linear extrapolations. All mobility calculations are performed with the scattering rates extrapolated to zero broadening.

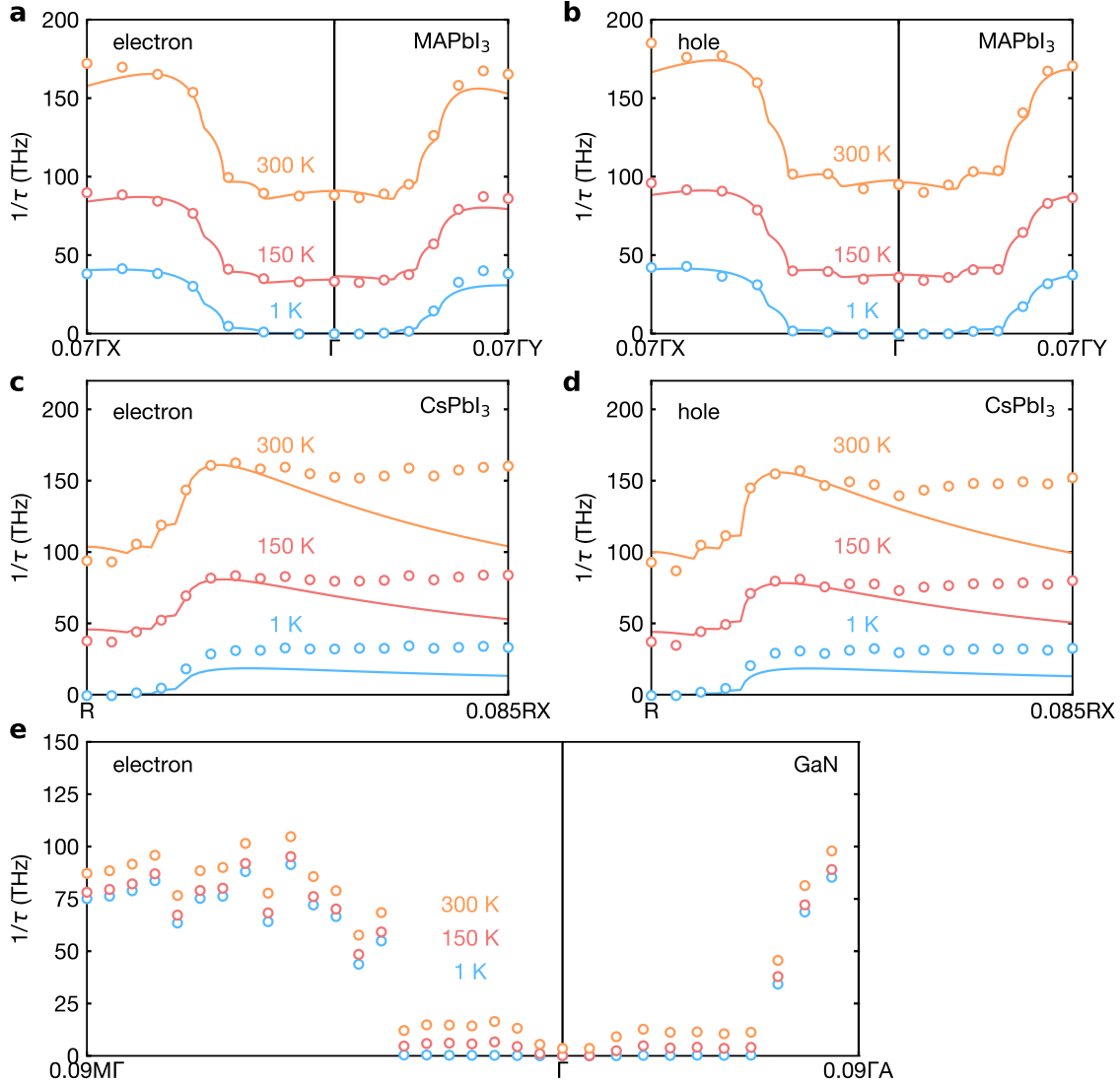


Figure S3: **Validation of the analytical interpolation: scattering rates.** (a-b) Calculated scattering rates of MAPbI₃ for electrons (a) and holes (b), at various temperatures. The circles indicate direct *ab initio* calculations using Eq. (2) of the manuscript, the lines are obtained from the analytical interpolation of Eq. (3). The two approaches agree closely for a range of temperatures. (c-d) Same as in (a-b), but for CsPbI₃. The deviation between the analytical interpolation and the direct calculations far from the *R* point is inconsequential for mobility calculations, as shown in Figure S4. (e) Computed scattering rates of electrons in GaN. In this case we calculate mobilities without resorting to the analytical interpolation of Eq. (3). The scattering rates are computed using 0 meV smearing for MAPbI₃ and CsPbI₃ (via extrapolation), and 1 meV smearing for GaN.

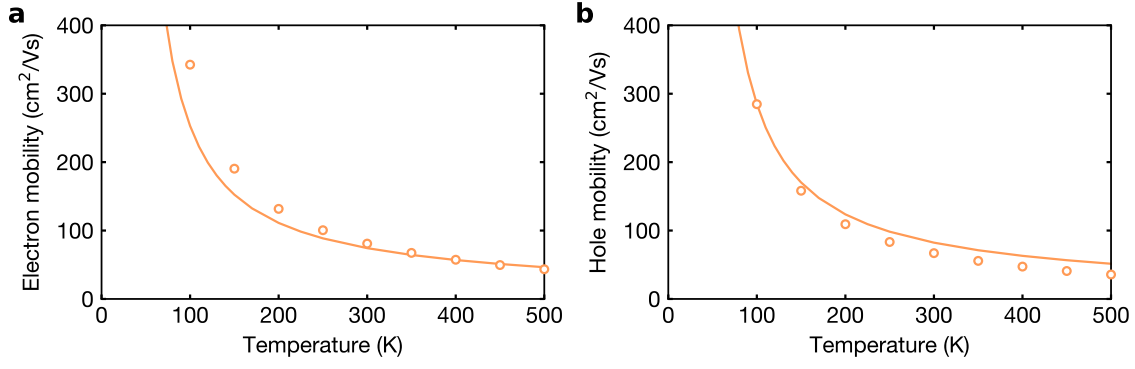


Figure S4: **Validation of the analytical interpolation: mobilities** (a) Electron mobility calculated for CsPbI₃ entirely from first principles (circles), and using the analytical interpolation of the scattering rates discussed in the Methods (lines). The close agreement between these results validates the interpolation methodology. (b) Hole mobility of CsPbI₃, calculated from first principles (solid line), or using the same interpolation technique as in (a).

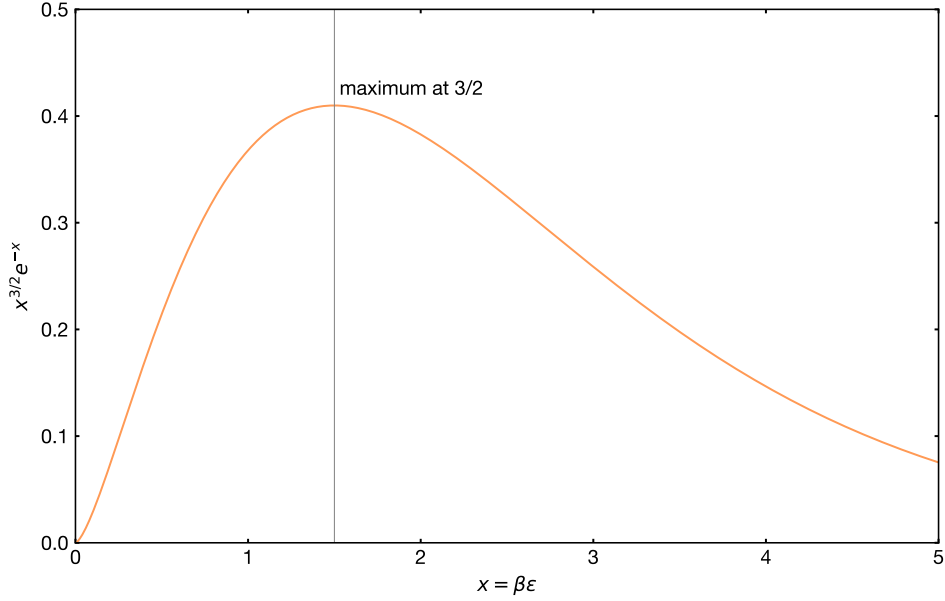


Figure S5: **Most representative electron energy.** In the simplified model developed in section 2 we need to evaluate the average scattering rate $\langle\tau\rangle = \frac{4}{3\sqrt{\pi}} \int_0^\infty dx x^{3/2} \exp(-x) \tau(x)$. Here we show that the weight factor $x^{3/2} \exp(-x)$ appearing in the integral peaks at $x = 3/2$, therefore the most representative electrons are those found at an energy $(3/2)k_B T$ from the band edge. This observation motivates our choice of focusing on electrons at this energy in Fig. 3 of the manuscript.

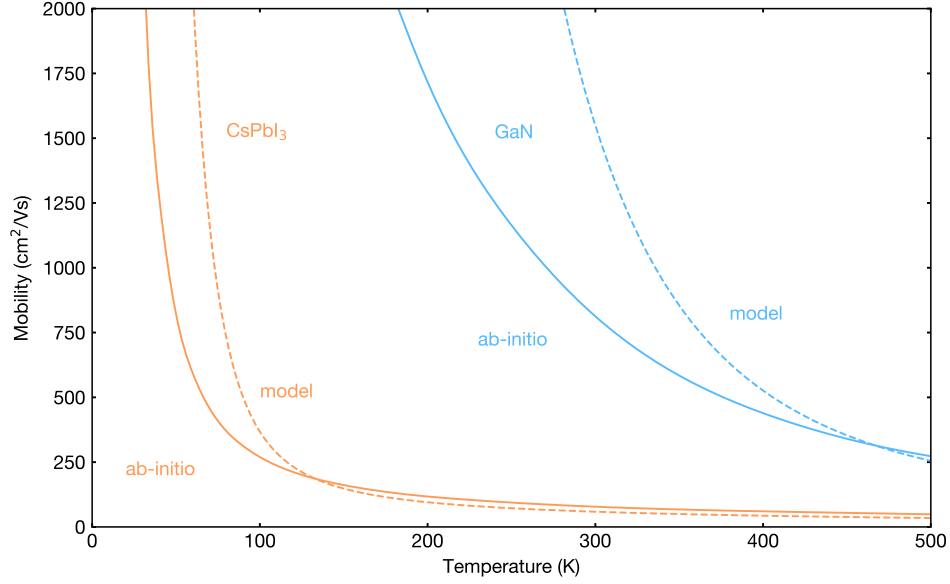


Figure S6: **Simplified mobility model vs. *ab initio* calculations.** We compare the carrier mobilities calculated for CsPbI₃ and for GaN using the simplified model of (S8) (dashed lines) with our first principles calculations (solid lines). In the case of CsPbI₃ we show the average electron and hole mobility, for GaN we show the electron mobility. Despite its simplicity, the model developed in section 2 captures qualitatively and semi-quantitatively the main trends observed in our complete *ab initio* calculations.

References

- 1 Fröhlich, H. Electrons in Lattice Fields. *Adv. Phys.* **1954**, *3*, 325.
- 2 Rohlfing, M.; Krüger, P.; Pollmann, J. Role of Semicore d Electrons in Quasiparticle Band-Structure Calculations. *Phys. Rev. B* **1998**, *57*, 6485–6492.
- 3 Filip, M. R.; Giustino, F. GW Quasiparticle Band Gap of the Hybrid Organic-Inorganic Perovskite $\text{CH}_3\text{NH}_3\text{PbI}_3$: Effect of Spin-Orbit Interaction, Semicore electrons, and Self-consistency. *Phys. Rev. B* **2014**, *90*, 245145.
- 4 Scherpelz, P.; Govoni, M.; Hamada, I.; Galli, G. Implementation and Validation of Fully Relativistic GW Calculations: Spin-Orbit Coupling in Molecules, Nanocrystals, and Solids. *J. Chem. Theory Comput.* **2016**, *12*, 3523–3544.
- 5 Giannozzi, P.; Andreussi, O.; Brumme, T.; Bunau, O.; Nardelli, M. B.; Calandra, M.; Car, R.; Cavazzoni, C.; Ceresoli, D.; Cococcioni, M.; et al., Advanced Capabilities for Materials Modelling with Quantum ESPRESSO. *Journal of Physics: Condensed Matter* **2017**, *29*, 465901.
- 6 Hamann, D. R. Optimized Norm-Conserving Vanderbilt Pseudopotentials. *Phys. Rev. B* **2013**, *88*, 085117.
- 7 van Setten, M.; Giantomassi, M.; Bousquet, E.; Verstraete, M.; Hamann, D.; Gonze, X.; Rignanese, G.-M. The PseudoDojo: Training and Grading a 85 Element Optimized Norm-Conserving Pseudopotential Table. *Comp. Phys. Comm.* **2018**, *226*, 39 – 54.
- 8 Baikie, T.; Fang, Y.; Kadro, J. M.; Schreyer, M.; Wei, F.; Mhaisalkar, S. G.; Graetzel, M.; White, T. J. Synthesis and Crystal Chemistry of the Hybrid Perovskite $(\text{CH}_3\text{NH}_3)\text{PbI}_3$ for Solid-State Sensitised Solar Cell Applications. *J. Mater. Chem. A* **2013**, *1*, 5628–5641.
- 9 Vurgaftman, I.; Meyer, J. R.; Ram-Mohan, L. R. Band Parameters for III-V Compound Semiconductors and their Alloys. *J. Appl. Phys.* **2001**, *89*, 5815–5875.

- 10 Mingo, N.; Stewart, D. A.; Broido, D. A.; Srivastava, D. Phonon Transmission through Defects in Carbon Nanotubes from First Principles. *Phys. Rev. B* **2008**, *77*, 033418.
- 11 Pérez-Osorio, M. A.; Milot, R. L.; Filip, M. R.; Patel, J. B.; Herz, L. M.; Johnston, M. B.; Giustino, F. Vibrational Properties of the Organic-Inorganic Halide Perovskite $\text{CH}_3\text{NH}_3\text{PbI}_3$ from Theory and Experiment: Factor Group Analysis, First-Principles Calculations, and Low-Temperature Infrared Spectra. *J. Phys. Chem. C* **2015**, *119*, 25703–25718.
- 12 Marini, A.; Hogan, C.; Grüning, M.; Varsano, D. Yambo: An *ab initio* Tool for Excited State Calculations. *Comp. Phys. Commun.* **2009**, *180*, 1392–1403.
- 13 Davies, C. L.; Filip, M. R.; Patel, J. B.; Crothers, T. W.; Verdi, C.; Wright, A.; Milot, R. L.; Giustino, F.; Johnston, M. B.; Herz, L. M. Bimolecular Recombination in Methylammonium Lead Triiodide Perovskite is an Inverse Absorption Process. *Nat. Commun.* **2018**, *9*, 293.
- 14 Godby, R. W.; Needs, R. J. Metal-Insulator Transition in Kohn-Sham theory and Quasiparticle theory. *Phys. Rev. Lett.* **1989**, *62*, 1169–1172.
- 15 Bruneval, F.; Gonze, X. Accurate *GW* Self-Energies in a Plane-Wave Basis Using Only a Few Empty States: Towards Large Systems. *Phys. Rev. B* **2008**, *78*, 085125.
- 16 Poncé, S.; Margine, E. R.; Verdi, C.; Giustino, F. EPW: Electron-Phonon Coupling, Transport and Superconducting Properties using Maximally Localized Wannier Functions. *Comp. Phys. Commun.* **2016**, *209*, 116–133.
- 17 Mostofi, A. A.; Yates, J. R.; Pizzi, G.; Lee, Y.-S.; Souza, I.; Vanderbilt, D.; Marzari, N. An updated Version of Wannier90: A Tool for Obtaining Maximally-Localised Wannier Functions. *Comp. Phys. Commun.* **2014**, *185*, 2309–2310.

- 18 Poncé, S.; Margine, E. R.; Giustino, F. Towards Predictive Many-Body Calculations of Phonon-Limited Carrier Mobilities in Semiconductors. *Phys. Rev. B* **2018**, *97*, 121201.
- 19 Schlipf, M.; Poncé, S.; Giustino, F. Carrier Lifetimes and Polaronic Mass Enhancement in the Hybrid Halide Perovskite $\text{CH}_3\text{NH}_3\text{PbI}_3$ from Multiphonon Fröhlich Coupling. *Phys. Rev. Lett.* **2018**, *121*, 086402.
- 20 Chen, H.-W.; Sakai, N.; Jena, A. K.; Sanehira, Y.; Ikegami, M.; Ho, K.-C.; Miyasaka, T. A Switchable High-Sensitivity Photodetecting and Photovoltaic Device with Perovskite Absorber. *J. Phys. Chem. Lett.* **2015**, *6*, 1773–1779.
- 21 Milot, R. L.; Eperon, G. E.; Snaith, H. J.; Johnston, M. B.; Herz, L. M. Temperature-Dependent Charge-Carrier Dynamics in $\text{CH}_3\text{NH}_3\text{PbI}_3$ Perovskite Thin Films. *Adv. Funct. Mater.* **2015**, *25*, 6218–6227.
- 22 Senanayak, S. P.; Yang, B.; Thomas, T. H.; Giesbrecht, N.; Huang, W.; Gann, E.; Nair, B.; Goedel, K.; Guha, S.; Moya, X.; et al., Understanding Charge Transport in Lead Iodide Perovskite Thin-Film Field-Effect Transistors. *Sci. Adv.* **2017**, *3*, e160193.